FULL PAPER

Three-Dimensional Kelvin Probe Microscopy for Characterizing In-Plane Piezoelectric Potential of Laterally Deflected ZnO Micro-/Nanowires

Dylan J. Bayerl and Xudong Wang*

Potential characterization of deflected piezoelectric nanowires (NWs) is of great interest for current development of electromechanical nanogenerators that harvest ambient mechanical energy. In this paper, a Kelvin probe microscopy (KPM) technique hybridizing scanning KPM (SKPM) with atomic force microscope (AFM) surface-approach spectroscopy methods for characterizing in-plane piezoelectric potential of ZnO microwires (MWs) is presented. This technique decouples the scanning motion of the AFM tip from sample topography, and thus effectively eliminates artifacts induced by high topographical variations along the edges of MWs/NWs which make characterization by conventional SKPM inappropriate or impossible. By virtue of the topography/tip motion decoupling approach, the electrical potential can also be mapped in a three-dimensional (3D) spatial volume above the sample surface. Therefore, this technique is named 3DKPM. Through 3DKPM mapping, the piezopotential generated by a laterally deflected ZnO MW was determined by extracting the potential asymmetry from opposite sides of the MW. The measurement results agree well with theoretical predictions. Integrating an external bias to the MW sample allowed direct observation of piezopotential and carrier concentration coupling phenomenon in ZnO, opening a door toward quantitative microscopic investigation of the piezotronic effect. With further positioning refinements, 3DKPM could become a powerful technique for the characterization of piezoelectric potential and related effects in micro/nanostructures of high topographical variations, as well as development of MW/NW-based piezoelectric nanodevices.

1. Introduction

Materials research in recent years has seen the rise and development of exciting applications for piezoelectric nanomaterials. Prototype nanowire (NW)-based nanogenerators have been demonstrated using a variety of piezoelectric materials including ZnO,[1–4] BaTiO$_3$,[5–7] Pb(Zr,Ti)O$_3$ (PZT),[8,9] and polyvinylidene fluoride (PVDF).[10,11] More importantly, coupling between the piezoelectric polarization and behavior of mobile charge carriers in ZnO NWs or microwires (MWs) has led to

a new concept for the operation of transistors,[12,13] sensors,[14–16] and optoelectronics.[17–19] With the conceptual bases proven experimentally, theoretical prediction and precise experimental characterization of the governing parameters of nanogenerators and piezotronic devices – in particular the piezoelectric potential produced by individual NWs – has become essential for further theoretical and technological development. Theoretical calculations have provided predictions of the piezoelectric potential from ZnO NWs/MWs under transverse deflection with/without considering the screening effect of mobile charge carriers.[13,20–24] Ferroelectric NWs were predicted to produce comparable or lower piezoelectric potential than semiconducting ZnO NWs because of their very high permittivity, despite having much higher piezoelectric coefficients.[24] Inhomogeneous strain in small-diameter NWs might lead to colossal enhancement of piezoelectric potential generation, known as the flexoelectric effect.[25,26] Shrinkage of the lattice constants by surface-structure domination for NWs a few nanometers in diameter could also enhance piezoelectric coefficients.[27] These intriguing theoretical predictions and their potential applications create great scientific desire to experimentally quantify the in-plane piezoelectric potential from deflected NWs/MWs.

Existing piezoelectric characterization methods either rely on inferring a piezoelectric potential based on the charge flow from/to a contacting electrode, e.g. a conductive atomic force microscopy (AFM) tip, to equilibrate the generated potential[4,7,28] or possibly by attempting to measure the surface potential on strained piezoelectric nanostructures by SKPM. Large uncertainty is introduced in the former by unknown electrode contact area, internal resistance, and surface potential distribution; and in the latter by systemic dependence of measured potential on SKPM operational parameters and a general class of measurement artifacts introduced by sample-topographical effects.[29–36] Experimental testing of theoretical predictions for piezoelectric potential generation by individual NWs/MWs has proven to be beyond the current capabilities of both electrode-based

D. J. Bayerl, Prof. X. D. Wang
Department of Materials Science and Engineering
University of Wisconsin-Madison
Madison, WI 53706, USA
E-mail: xudong@engr.wisc.edu

methods and SKPM, due to the challenging electrode incorporation on 1D structures and their high topographical variation, respectively. We therefore devised 3DKPM to transcend these limitations and enable artifact-free surface potential mapping of high topography surfaces. The technique is employed here to demonstrate direct measurement of the piezoelectric potential generated by individual ZnO MWs and to observe potential screening by mobile charge carriers.

2. Origins of Topography-Induced Artifacts in SKPM

Since its development, SKPM has been the standard scanning AFM method for surface potential measurements. In this technique, both a DC voltage (V_{DC}) and an AC voltage (V_{AC}) with angular frequency ω are applied to a conductive AFM tip as it is raster scanned over a sample surface. The oscillating potential difference between the tip and surface results in an oscillating electrostatic force of the form

$$F = K(z)[V_{DC} - V(z)]V_{AC}\sin(wt) \tag{1}$$

where $K(z)$ and $V(z)$ are the tip-surface capacitive coupling and potential, respectively. The capacitive coupling $K(z)$ has been shown to depend on tip, cantilever, and surface geometry, as well as average tip-surface distance z.[31–41] Note that $K(z)$ determines the form of the point spread function with which $V(z)$ is convolved to produce an SKPM image.[32,37,40,42–44] While deconvolution processes are required for truly quantitative measurement of surface potential, we neglect this consideration at present to focus on applicability of 3DKPM to high-topography surfaces. The potential $V(z)$ is then simply considered the weighted average of local potential in the vicinity of the apex of the AFM tip at tip-surface distance z,[29,32,38,43] and has the general form

$$V(z) = G(z)[V_{abs} + (\chi_{tip} - \chi_s)] \tag{2}$$

depending on absolute surface potential V_{abs} and the difference between the electron affinities and/or work functions of the tip and sample surface ($\chi_{tip} - \chi_s$). The z dependence of $V(z)$ arises from scaling by a function $G(z)$, which decays approximately as the Coulomb potential such that $G(0) = 1$ and $G(z \to \infty) = 0$, meeting external electrostatic boundary conditions of the sample. During sample scanning, a feedback loop adjusts V_{DC} to minimize V_{AC} induced tip oscillation at frequency ω, corresponding to the condition $V_{DC} = V(z)$ by Equation 1. If the feedback loop perfectly nullifies F, and z is held constant at all points in the sample scan, SKPM maps $V(z)$ on the sample surface. If ($\chi_{tip} - \chi_s$) is also constant, variation in $V(z)$ corresponds to relative difference in the scaled absolute potential $G(z)V_{abs}$, which converges on V_{abs} with arbitrarily small z. In practice, however, there typically exists a nonzero tracking error in the V_{DC} feedback loop,[39,45] introducing error as $V_{DC} = (V(z) + V_{error})$. The magnitude of V_{error} increases when $V(z)$ changes rapidly, such as with discontinuities in V_{abs} or ($\chi_{tip} - \chi_s$) at ferroelectric domain boundaries, monolayer growth step edges, and metal-semiconductor junctions.[30,32,34–38,45] Furthermore, the finite response time of the feedback loop holding z constant has a nonzero tracking error, introducing additional error as $V_{DC} =$

$[V(z + z_{error}) + V_{error}]$ if there are variations in topography of the surface. As a final consideration, if the tracking error in the constant-z feedback loop is large enough (e.g., at discontinuous topography boundaries such as the edge of a MW/NW), the oscillating tip can impact the surface, which significantly perturbs oscillations and further disrupts the F-nullifying feedback loop. Reducing the velocity of the tip during raster scanning mitigates these tracking errors, but was found to be insufficient to guarantee artifact-free imaging when sample topography exhibits significant discontinuous variations of ~100 nm or more. A typical SKPM image of a ZnO NW is included in the Supporting Information (Figure S1), showing artifacts due to the discontinuous NW topography. Such artifacts are magnified in the case of MWs by larger topography variation. These four sources of error in SKPM measurements – the z dependence of $V(z)$, the V_{DC} tracking error V_{error}, the constant height tracking error z_{error}, and surface contact error – make mapping of V_{abs} challenging. By Equation 2, exact measurement of V_{abs} requires precise knowledge of both $G(z)$ and ($\chi_{tip} - \chi_s$), as well as methods to eliminate V_{error} and z_{error}. 3DKPM was developed in order to address these challenges and thus enable the characterization of in-plane potential generated by deflected piezoelectric wires.

3. The 3DKPM Technique

3DKPM can simultaneously eliminate V_{error}, z_{error}, and surface contact error while enabling direct observation of $G(z)$ scaling, and is demonstrated for characterizing the piezoelectric potential of ZnO MWs free of artifacts. 3DKPM is also applicable to surfaces or structures where high topography variation introduces artifacts in SKPM images. In our experimental arrangement, dependence of piezoelectric potential measurements on positional variations in $K(z)$ and ($\chi_{tip} - \chi_s$) is effectively negated by comparing the relative potential between geometrical mirror-image points on opposite sides of MW samples. 3DKPM entails scanning a mechanically oscillated conductive AFM tip through a spatial volume containing the surface and nanostructure of interest (**Figure 1**a). Rather than raster scanning in the plane of the surface as with conventional scanning probe techniques, a fine grid of points is specified on the surface and the tip is gently approached toward the surface at each point, effectively decoupling tip motion from sample topography and eliminating artifacts from constant-z feedback loop tracking error (z_{error}). A grid of 25 to 50 nm periodicity is typical of and sufficient for our experiments, yet the lower limit is equivalent to the lateral positioning precision of the AFM apparatus (~1 nm). As in SKPM operation, V_{DC} and V_{AC} with angular frequency ω are applied to the conductive tip and an F-nullifying feedback loop adjusts V_{DC} to equal $V(z)$ as in Equation 1. With the tip gently approaching the surface instead of raster scanning across it, $V(z)$ varies smoothly as $G(z)$ instead of discontinuously with $[V_{abs} + (\chi_{tip} - \chi_s)]$ from Equation 2, greatly reducing or eliminating V_{error}. $V(z)$ is thus obtained at each grid point on and above the sample surface. With the dominant scanning direction vertical rather than lateral, eliminating surface contact error requires only truncation of $V(z)$ before the tip touches the surface. Mechanical oscillation of the AFM tip near its resonant frequency provides a means to determine the z position just

**ADVANCED
FUNCTIONAL
MATERIALS**

www.afm-journal.de

Materials Views

www.MaterialsViews.com
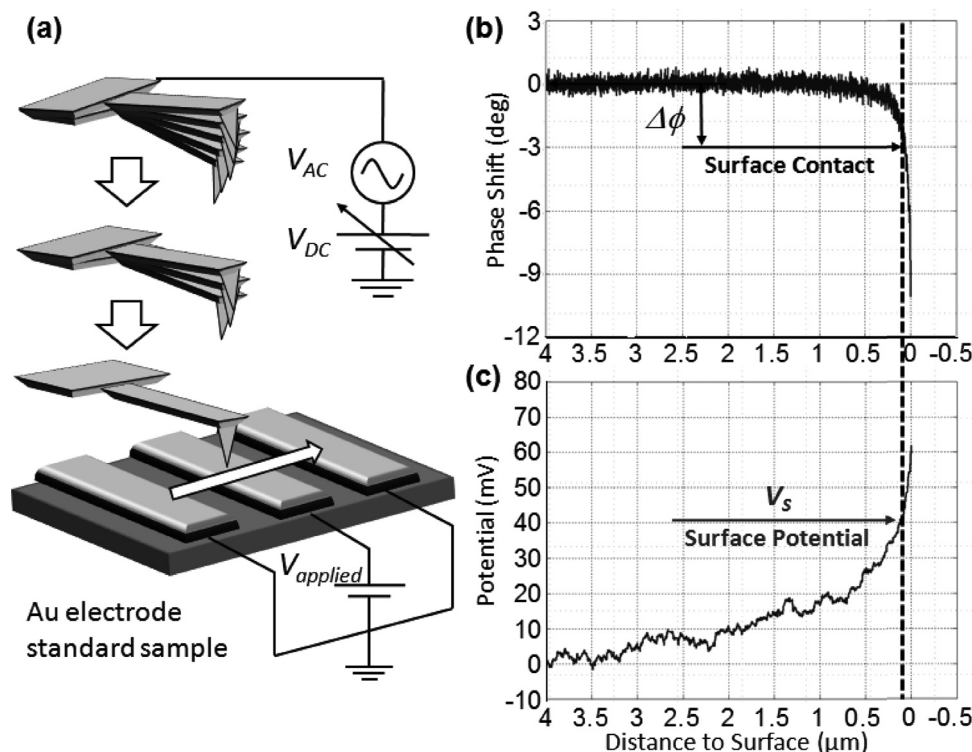
Figure 1. 3D Kelvin probe microscopy (3DKPM) technique. a) Schematic of the 3DKPM characterization process. Instead of scanning laterally, the AFM tip is lifted far above sample surface and then moved downward until physical contact was made with sample surface. The potential and AFM tip oscillation phase are recorded simultaneously. The surface potential is determined by identifying the point just before AFM tip contacts sample surface. The AFM tip is then moved to the next position on the sample surface and the process is repeated. b,c) Tip oscillation phase (ϕ) and potential curve V_{DC} recorded during descent of AFM tip. Empirical study of tip oscillation during approach showed that when tip-surface forces induce a phase shift of $\Delta\phi = 3°$ the tip is near the surface without touching. The corresponding potential value is determined as the surface potential V_S. The part of the potential curve at larger positive distance-to-surface is the potential distribution $V(z)$ in space above sample surface.

before the tip contacts the surface (z_0). The phase shift (ϕ) of tip oscillation at its mechanically driven frequency (ω_d), approximated as a 1-degree-of-freedom driven, damped harmonic oscillator is given by[46]

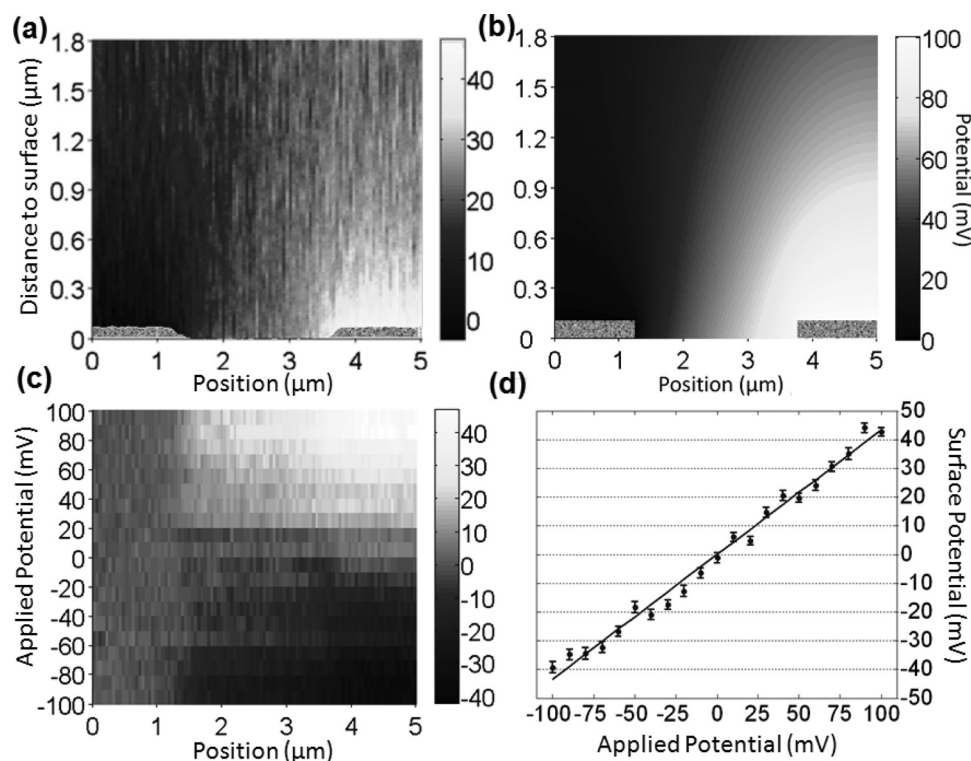$$\phi = \arctan[(\omega_f \omega_d/Q)/(\omega_f^2 - \omega_d^2)] \qquad (3)$$

where Q is the quality factor and ω_f is the effective resonant frequency of the AFM tip. Q is a constant depending on the atmosphere and AFM tip-cantilever system, while $\omega_f = \{[k-f(z)]/m\}^{1/2}$, where k and m are the Hookean spring constant and effective mass of the simplified tip-cantilever system, respectively, and $f(z)$ describes the gradient of tip-surface interaction forces. Far from the surface, force gradients are weak and $f(z)$ becomes vanishingly small, but short range van der Waals interactions cause $f(z)$ to increase rapidly near z_0. By Equation 3, ϕ therefore remains approximately constant (ϕ_0) at large z and changes rapidly near z_0 (Figure 1b). A characteristic shift ($\Delta\phi$) in oscillation phase from ϕ_0 must be determined experimentally to reveal close tip-surface proximity just before surface contact.[47–49] For our AFM apparatus operating in atmosphere at room temperature, $\Delta\phi = 3°$ was determined by an empirical approach comparing an ensemble of several hundred 3DKPM experiments over a variety of operating conditions and test samples. The truncation point to obtain $V(z)$ (Figure 1c) without surface contact error is then dictated by $\Delta\phi$, as shown by the dashed line in

Figure 1b and c. The surface potential obtained by 3DKPM (V_S) is then defined as $V_S = V(z_0) = G(z_0)[V_{abs} + (\chi_{tip} - \chi_s)]$, i.e., at the closest possible proximity to the surface without introducing errors from surface contact. The potential curve $V(z)$ measured at larger z above the surface (the portion on the left of V_S in Figure 1c) can then be considered as the approximate spatial potential distribution above the approached point on the sample surface when neglecting deconvolution. Combining $V(z)$ from the entire grid of points on the sample surface provides a full 3D map of the spatial potential distribution induced by surface potential on the sample in the scan volume. While 3DKPM may obtain 3D potential maps of the scan volume, the approximate longitudinal symmetry of the MW morphology allows suppression of one grid dimension for simplicity of representation in print. 2D potential maps in the vertical plane extending above the sample surface (representing a vertical slice of a 3D scan volume) were therefore acquired without loss of essential experimental features.

4. Calibration of 3DKPM for Surface Potential Measurement

The ability of the 3DKPM technique to map a spatial potential distribution was first verified on a standard sample consisting of an interdigitated Au electrode pair on a GaAs substrate. One

Materials
Views
www.MaterialsViews.com

ADVANCED
FUNCTIONAL
MATERIALS
www.afm-journal.de

FULL PAPER

Figure 2. 3DKPM characterization of Au electrode standard sample. a) Spatial potential distribution quantified by 3DKPM on two standard Au electrodes. Electrode on left-hand-side (white space from 0 to 1.25 μm) was grounded and constant voltage of 100 mV was applied to electrode on right-hand-side (white space from 3.75 to 5 μm). b) Simulated potential distribution between two standard Au electrodes showing very close agreement with potential distribution measured by 3DKPM. c) Surface potential V_S between two electrodes, where applied voltage was changed from −100 mV to 100 mV on right electrode with left electrode kept at ground. d) Plot of averaged V_S ($V_{S,mean}$) on the right electrode determined by 3DKPM versus applied potential. Error bars are the standard deviation of V_S on the right electrode. The linear relationship shows that the 3DKPM technique accurately quantifies surface potential of charged surfaces. The difference between the magnitudes of applied and measured surface potentials are due to Coulomb potential decay by $G(z_0)$ at nonzero tip-sample distance. The reciprocal of the slope of the first-order interpolant gives the scaling correction factor $1/G(z_0) = 2.2$.

electrode was grounded to the AFM chassis by a shielded cable while the other was connected to a precision DC voltage source providing controllable V_{abs} (Figure 1a). Since the magnitude of V_{abs} is determined arbitrarily by the relative ground potentials of the AFM tip, chassis, and precision DC voltage source, only relative differences in $V(z)$ between scan volume coordinates are quantitatively measured. The averaged V_S measured on the ground electrode by 3DKPM was normalized to 0 V. **Figure 2**a shows the spatial potential distribution in a plane bisecting a single pair of adjacent electrode fingers, where the left electrode was grounded and a 100 mV DC bias was applied to the right one. The underlying GaAs substrate is exposed in the gap between the electrodes, contributing nonzero $(\chi_{tip}-\chi_s)$. The superposition property of electrostatic potentials allows $(\chi_{tip}-\chi_s)$ to be subtracted (see the Supporting Information, Figure S2) such that $G(z_0)V_{abs}$ surrounding the electrodes can be quantitatively mapped. With V_S on the grounded electrode normalized to 0 mV, V_S on the 100 mV DC biased electrode was found to be ~45 mV. The deviation of this measured surface potential from the applied 100 mV can be absorbed by the Coulomb potential scaling factor $G(z_0)$. A finite element simulation of the electrode standard sample was performed to pre-

dict the spatial potential distribution. As shown in Figure 2b, a qualitatively identical potential distribution was obtained without considering the potential scaling factor $G(z)$ (primarily affecting potential magnitude) or convolution due to $K(z)$ (primarily affecting spatial features of the potential distribution). While deconvolution of the potential map may be necessary for high precision quantitative measurement of smaller-scale surface features, it is neglected here for simplicity. This simulation demonstrates that, provided $G(z)$ is taken into account, 3DKPM can accurately map the electric potential $V(z)$ in a 3D space with an electric potential gradient resolution of at least 5 mV per 50 nm.

To insure accurate detection of variable surface potentials, it was necessary to confirm that V_S scales linearly with V_{abs}. The linearity of 3DKPM response to varying surface potential was calibrated by applying a progression of DC biases to the right electrode whilst keeping the left electrode at ground. The DC bias was varied over a range of −100 to +100 mV with 10 mV increments. Figure 2c summarizes the difference of V_S between the ground and biased electrodes at different bias voltages. The ground electrode (located from 0 to 1.25 μm) exhibited a consistent surface potential, which was normalized to 0 V as a
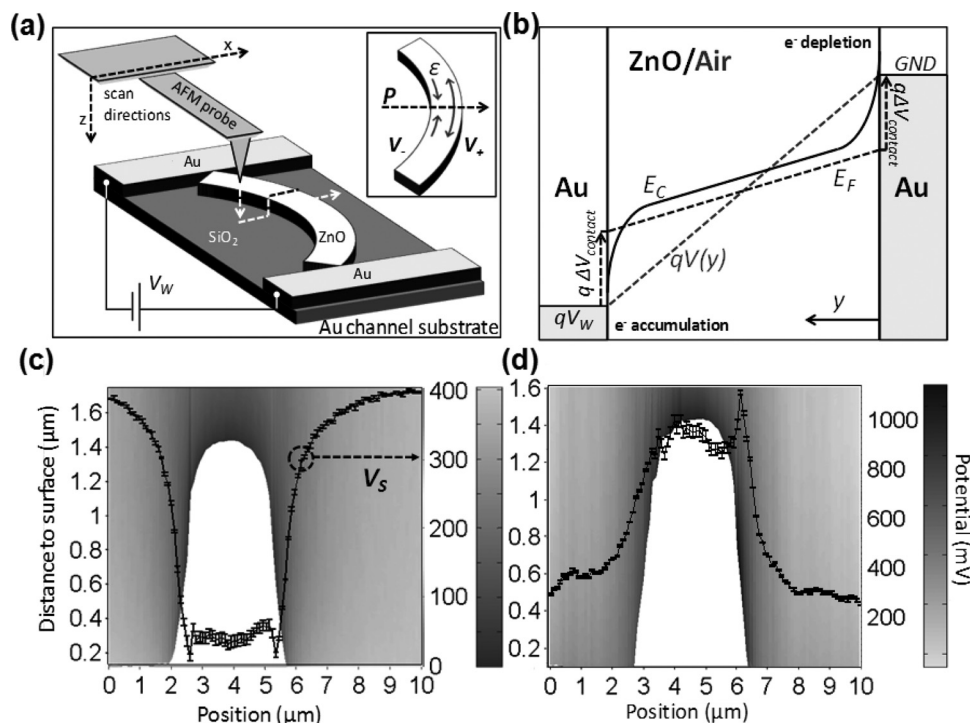
Figure 3. 3DKPM characterization of piezoelectric potential on ZnO MWs. a) Schematic experimental setup for measuring piezoelectric potential on strained ZnO MW. Inset shows relation between bending direction, compressive/tensile strain (ε) on concave/convex sides, resultant piezoelectric polarization vector (**P**), and lower (**V$_-$**)/higher (**V$_+$**) relative potentials on either side of the MW. b) Influence of V_{MW} on electronic structure of ZnO MW. Contact resistance between ends of ZnO MW and Au electrodes results in interfacial voltage drop ($\Delta V_{contact}$) and Fermi level mismatch between Au electrodes and ZnO. The electric potential in air outside ZnO MW ($qV(y)$) has a steeper gradient than ZnO Fermi energy, resulting in depletion/accumulation of excess free charge near GND/V_{MW} electrode. 3DKPM potential maps of strained ZnO MW near V_{MW} (c) and GND (d) electrodes. Central white region shows location of axial cross-section of the MW. Surface potential V_S is extracted from the potential maps and overlain in black, corresponding to potential scales on the right-hand-side. Error bars are the standard deviation of V_S averaged from $V(z_0)$ to $V(z_0 + 10$ nm) to smooth noise from V_{DC} ripple of ~5 mV. In (c) V_S near the V_{MW} electrode is clearly lower than background potential while the opposite is true in (d) near the GND electrode. V_S is the same on stretched and compressed sides of the MW near V_{MW} electrode (c) where accumulated mobile charge carriers screen piezoelectric potential. A large positive spike in V_S is observed on stretched (right) side near the GND electrode (d) where mobile charge carriers are depleted.

reference. V_S measured on the biased electrode (located from 3.75 to 5 μm) exhibited ~-45 mV to ~$+45$ mV compared to the ground electrode as V_{abs} was adjusted from -100 to $+100$ mV. The V_S distribution between electrodes exhibited a smooth gradient from the ground to the biased electrode. V_S on the biased electrode surface was averaged as the mean value ($V_{S,mean}$) to represent potential on the biased electrode, which was then plotted versus the applied potential V_{abs}. As shown in Figure 2d, $V_{S,mean}$ followed a linear dependence on applied DC bias, indicating high precision measurement of $G(z_0) V_{abs}$ with no appreciable nonlinear response to variation in surface potential. An approximate scaling factor $[1/G(z_0)] = 2.2$ was calculated from the $G(z_0) V_{abs}$ vs. V_{abs} curve. The scaling factor allows conversion of measured surface potential V_S to an approximated surface potential $V_S^* = [V_{abs} + (\chi_{tip} - \chi_s)] = [V_S/G(z_0)]$ when V_S is obtained from $V(z)$ using truncation parameter $\Delta\phi = 3°$ on the Au electrode standard sample. While the exact value of $1/G(z_0)$ certainly depends on surface topography due to the variation of $K(z_0)$, this conversion is applied without further refinement to the following characterization experiments as a suitable first-order correction.

5. Characterization of Piezoelectric ZnO MWs by 3DKPM

With the capability for high-resolution surface potential mapping established, 3DKPM was applied to characterize the piezoelectric potential in ZnO MWs. Individual ZnO MWs were dispersed on a Si substrate and then manipulated by AFM to fit into a test structure. The structure consisted of a SiO$_2$ substrate with two thick (3.5 to 4.5 μm) Au electrode bars, resulting in a channel of bare SiO$_2$ between Au sidewalls. The ZnO MW was then manipulated into a bent configuration and held by the sidewalls of the Au electrodes (Figure S3 in the Supporting Information).

The 3DKPM characterization of a bent ZnO MW is schematically shown in **Figure 3**a. Potential maps were acquired transverse across the axis of the wire in ambient atmosphere and at room temperature. ZnO MWs grown via our CVD process were known to have high n-type doping concentration (~10^{17} cm^{-3}), which was expected to largely cancel the piezoelectric potential due to mobile charge carriers accumulating near the polarized surfaces.[21,22] To resolve potential generated by piezoelectric

www.MaterialsViews.com

ADVANCED
FUNCTIONAL
MATERIALS
www.afm-journal.de

FULL PAPER

polarization without cancellation by mobile carrier redistribution effects, a DC bias of $V_{MW} = 5$ V was applied along the MW between Au electrodes. Figure 3b shows the influence of V_{MW} on the electronic structure of the ZnO MW. A nonzero contact resistance at one or both ZnO/Au interfaces[50,51] reduces the gradient of the electronic potential inside ZnO relative to that in the surrounding atmosphere. This results in mobile carrier accumulation in the MW near the anode and depletion near the cathode, allowing unscreened piezoelectric potential from fixed dipoles to be observed. Potential maps acquired near the V_{MW} electrode (*GND* electrode) in Figure 3c (Figure 3d) clearly show a surface potential V_S of the ZnO MW ~350 mV lower (~550 mV higher) than the background V_S, indicating local accumulation (depletion) of negative charge carriers. Note that V_S shown in Figures 3c and d may be multiplied by $1/G(z_0) = 2.2$ to estimate the actual surface potential V_S*. The V_S profiles superimposed on Figures 3c and d reveal that only when mobile carriers were depleted could distinguishable piezoelectric potential be detected from the MW. No piezoelectric potential was detected in potential maps acquired in the accumulation region of the MW near the V_{MW} electrode, or anywhere in the wire when V_{MW} = GND, in agreement with the mobile carrier redistribution model. Screening of piezoelectric potential with high carrier concentration and emergence of strong piezoelectric potential with carrier depletion reveal the redistribution of mobile charge carriers in ZnO MW in order to equilibrate strain-induced polarization, which was consistent with a coupling effect between the piezoelectricity and semiconductor properties.
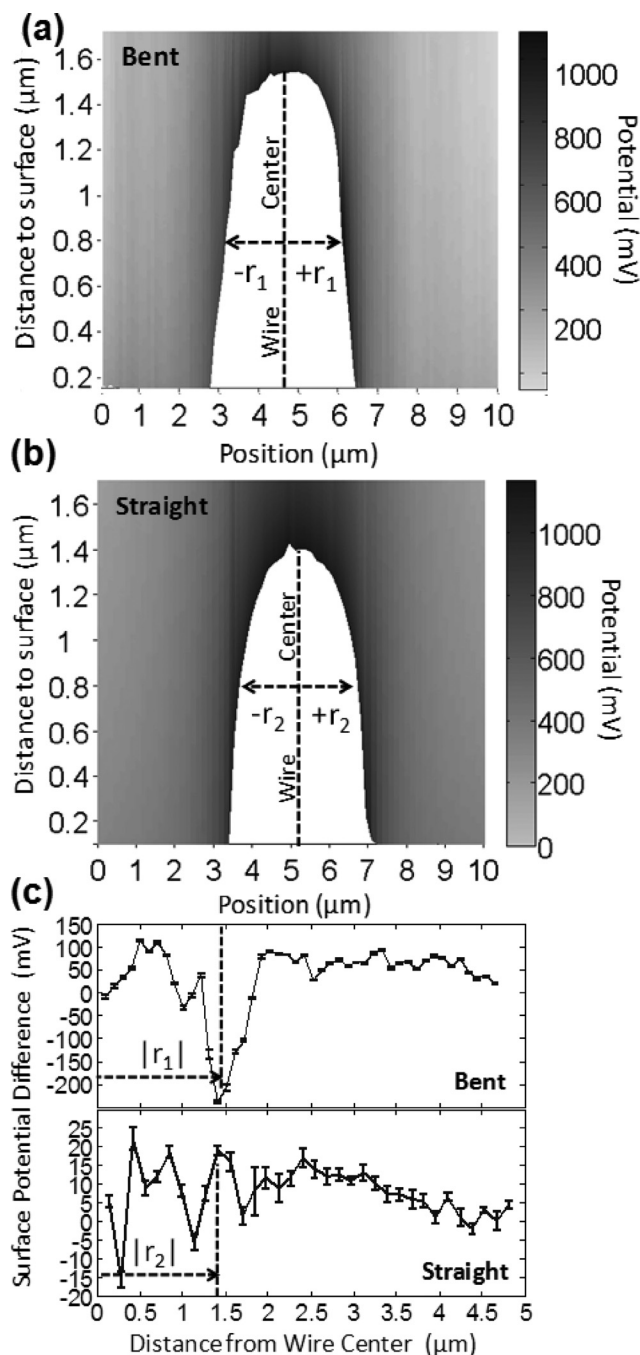
5.1. ZnO with Mobile Carrier Depletion

To observe the largest possible piezoelectric potential with minimal screening from mobile carriers, characterizations were conducted by acquiring 3DKPM potential maps near the GND electrode. **Figure 4**a is the potential map of a bent ZnO MW, where the asymmetry in the potential distribution between the left/compressed and right/stretched sides is apparent near the surface of the MW. A relatively higher potential on the stretched side is in agreement with theoretical predictions.[20–24] The smooth spatial potential distributions and high fidelity to sample topography indicate that 3DKPM is able to detect small variations in surface potential without introducing artifacts from large topographical variations, as would be unavoidable with SKPM under similar conditions.

To insure that the asymmetry in the potential distribution can be attributed to piezoelectric polarization, the same ZnO MW was measured in a strain-free condition (Figure S3 in the Supporting Information). Figure 4b shows the 3DKPM potential map of the straight MW. Very little asymmetry was observed in the potential distribution between opposite sides of the straight MW compared to the case of the bent MW. This confirms that piezoelectric potential generated on the side surfaces of the bent MW can be directly detected by the 3DKPM approach.

5.2. Extracting Piezoelectric Potential from 3DKPM Measurements

To determine the actual piezoelectric potential generated by bent ZnO MWs, the asymmetry in the potential distribution


Figure 4. 3DKPM potential maps of ZnO MWs and method of extracting piezoelectric potential. Potential maps of a ZnO MW characterized under mobile charge carrier depletion condition when bent (a) and straight (b). The white space indicates the axial cross section of the MW. Asymmetric potential distribution near the surface can be clearly observed from the bent MW due to piezoelectric polarization with relatively higher (lower) potential on the stretched/right (compressed/left) side. The wire center is found based on topography of cross section (the white space), with equal distance ($\pm r_1$, $\pm r_2$) from each side to the center. Potential difference at distance $\pm r$ from the wire center measures asymmetry in potential distribution $\Delta V_S(r)$. Surface potential difference between both sides of MW at position $|r_{side}| = |r_1|$, $|r_2|$ yields the reduced piezoelectric potential $G(z_0) V_{piezo}$. c) Calculated $\Delta V_S(r)$ from potential maps of bent (a) and straight (b) ZnO MW. Error bars are computed for $\Delta V_S(r)$ as they were for V_S in Figure 3c and d.

was extracted from the background potential. Since both the MW cross-section and the AFM tip share a geometrical symmetry plane, the position of the MW center was determined as the position of the topographical mirror plane, as indicated by the dashed lines in Figure 4a and b. The asymmetry in the surface potential was then calculated at each distance $|r|$ from the wire center as $\Delta V_S(r) = [V_S(\text{center} - r) - V_S(\text{center} + r)]$. Calculated $\Delta V_S(r)$ from the bent and straight ZnO MW potential maps shown in Figure 4a and b are plotted in Figure 4c. Piezoelectric potential was determined from the surface potential asymmetry corresponding to the side surfaces $|r_{side}|$ of the ZnO MWs scaled by $1/G(z_0)$, i.e., $V_{piezo} = \Delta V_S^*(r_{side}) = \Delta V_S(r_{side})/G(z_0)$. For the bent and straight ZnO MW shown in Figure 4, $|r_{side}| = |r_1|$ and $|r_2|$, respectively. Through this method, surface potential asymmetry of $\Delta V_S(r_1) = -220$ mV was extracted from the ΔV_S profile shown in Figure 4c, yielding a piezoelectric potential $V_{piezo} = -480$ mV between compressed and stretched surfaces of the bent wire; while V_{piezo} on the straight MW could not be distinguished from noise or background potential asymmetry. The nonzero surface potential asymmetry observed in the background (away from $|r_{side}|$) may be attributable either to nonuniformities in the intrinsic surface potential of the substrate or imperfect alignment of the acquired potential maps with equipotential surfaces of the spatial potential induced by the Au electrodes. The presence of either factor would contribute to nonzero background potential asymmetry. However, these contributions must be minimal near $|r_{side}|$ where V_S on the side surfaces dominates as long as the magnitude of the background potential asymmetry is significantly less than that of the MW potential asymmetry. Error bars do not account for this background potential asymmetry due to the uncertainty in its exact magnitude and origin.

Piezoelectric potential generated by the ZnO MW in the Au electrode channel was measured in two separately manipulated but geometrically similar bending configurations to verify the repeatability of 3DKPM characterization, as well as a straight configuration for reference. The results are summarized in **Figure 5**. At different positions on the MW, V_{piezo} between 350 and 480 mV were detected in the first bending condition, and between 420 and 600 mV in the second bending condition. The significant shifting of V_{piezo} is likely due to variations in both strain and local carrier depletion conditions. Uncertainty in the exact position on the MW and in the Au electrode channel at which 3DKPM potential maps were obtained after sample and MW manipulations precludes comparison of these data independent of these factors. This limitation could be addressed by more precise NW positioning strategies. The unstrained configuration produced no V_{piezo} distinguishable from noise or background potential asymmetry.

To insure that measured piezoelectric potentials were not caused by asymmetric sensitivity of the conductive AFM tip to electrostatic forces, additional 3DKPM measurements were performed for each bending configuration after rotating the entire sample by 180°. This maneuver interposed the stretched and compressed sides of the wire relative to the orientation of the AFM tip. Following the V_{piezo} determination procedure described previously, the expected and obtained result was sign inversion of V_{piezo} without significant change in magnitude. We therefore conclude that asymmetry in the potential map obtained by 3DKPM was solely produced by the piezoelectric
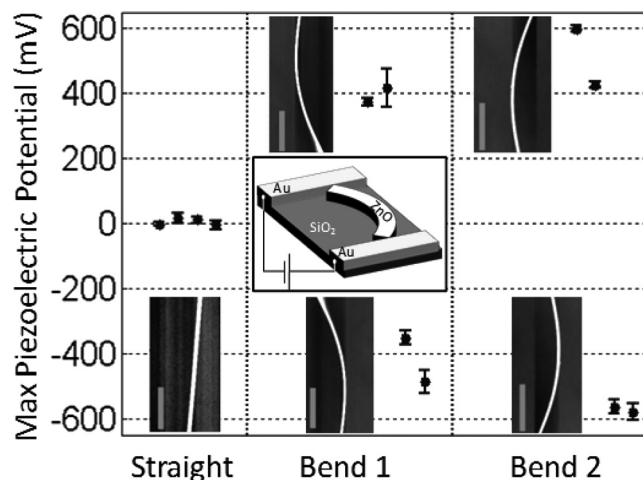
Figure 5. Piezoelectric potential characterization of ZnO MWs with multiple bending configurations. Piezoelectric potential $V_{piezo} = [\Delta V_S(r_{side})/G(z_0)]$ measured on ZnO MWs confined between Au electrodes under mobile charge depletion condition (inset). Wire was reoriented by 180° in each bending condition and re-measured to show flipping of sign of V_{piezo} without changing magnitude, demonstrating independence of measured V_{piezo} from MW orientation relative to AFM tip. Insets corresponding to each data point group are AFM topography images showing bending conditions of ZnO MW and relative orientation (all scale bars are 10 μm).

potential of the ZnO MW, without any artifacts introduced by the shape or sensitivity of the AFM tip.

6. Conclusion

A novel 3DKPM technique was developed for artifact-free mapping of the potential distribution on surfaces with large topography variations. This unique merit is ideal for precisely characterizing surface properties of individual micro/nanostructures where topography-induced measurement artifacts were previously of significant concern. 3DKPM was applied to characterize the piezoelectric potential generated by laterally strained ZnO MWs by extracting the potential asymmetry from opposite sides of the MW. A reliable basis for quantifying the piezoelectric property of 1D micro/nanostructures was thus demonstrated, and the possibility of directly visualizing the piezopotential-size-strain relationship in these structures is implicated. Refinements to the 3DKPM technique such as deconvolution of the spatial potential map, detailed experimental study of Coulomb scaling parameter $G(z)$, and modeling the form of electrostatic force $F(z)$ in the presence of high topography variation are expected to improve quantitative precision and enable highly accurate experimental testing of theoretical predictions. Integrating an external bias to the MW sample allowed direct observation of piezopotential and carrier concentration coupling phenomenon in ZnO, opening a door toward quantitative microscopic investigation of the piezotronic effect. 3DKPM therefore has the potential to become a useful addition to the ensemble of SPM techniques and surface potential characterization methods, especially for the characterization of piezoelectric potential and related effects in micro/nanostructures of high topographical variations, as well as development of MW/NW-based piezoelectric nanodevices.

Materials
Views
www.MaterialsViews.com

ADVANCED
FUNCTIONAL
MATERIALS
www.afm-journal.de

FULL PAPER

7. Methods

ZnO MW Synthesis: ZnO MWs were grown by chemical vapor deposition in a temperature-gradient tube furnace. Pure ZnO powder was used as the precursor and located at the center of an alumina tube. Cooling collars were installed on the two ends of the alumina tube to insure a large temperature gradient. Ar atmosphere with a constant flow rate of 50 sccm was maintained inside the tube and the pressure was kept at ~200 Pa. The system was heated to 1400 °C with a heating rate of 50 °C/min and kept at that temperature for 30 minutes. A polycrystalline alumina substrate was located 10 cm away from the powdered ZnO source, covering a deposition temperature range from ~300 °C to ~500 °C. Micrometer wide and nearly millimeter long ZnO wires were produced on the polycrystalline alumina substrate. ZnO wires were then collected and dry-dispersed on an 8 mm × 8 mm Si wafer for AFM manipulation and 3DKPM characterization.

Au Channel Substrate Fabrication: Au channel substrate for 3DKPM characterization was fabricated on [001] intrinsic Si wafer. A ~500 nm insulating native oxide layer was first grown on Si by wet oxidation, followed by masking of the Au electrode pattern by standard lithographic processes. Au electrode bars were deposited by CHA-600 e-beam evaporator to a thickness of ~4 μm and the mask was subsequently dissolved. 0.25 mm Cu/Sn wires for connection to an external voltage source were then bonded to each electrode pad with Ag paste. Resistance between external Cu wire connections and associated Au electrodes was <0.3 Ω while resistance between Au electrodes exceeded 200 MΩ, insuring that Au electrodes could be independently biased.

Configuration of AFM for 3DKPM: The 3DKPM apparatus was based on a commercial AFM (Park Systems XE-70) equipped for SKPM and surface-approach spectroscopy modes. Heavily doped Si AFM cantilevers with 20 nm Au conductive coating and 20 nm Cr underlayer (MikroMasch NSC14/Cr-Au) were used for potential mapping. An external phase-sensitive lock-in amplifier (Stanford Research Systems SR8340 DSP) was configured for KPM operation and used to apply $V_{AC} = 2.5$ V at 18 kHz driving frequency to the AFM tip and extract induced tip oscillation phase and amplitude. The V_{DC} feedback loop and lock-in amplifier filtering parameters were optimized empirically on an Au/Ti/GaAs interdigitated electrode sample to minimize noise and $V(z)$ tracking errors for tip scanning velocity of 300 nm/s. This scanning velocity was then used for 3DKPM surface approach at grid positions spaced 25 to 50 nm apart.

Surface approach truncation parameter $\Delta\phi$ for determining minimum tip-sample distance z_0 to prevent surface contact error in V_S was determined empirically by two experimental methods establishing lower and upper limits on $\Delta\phi$. The first method determined the lower limit by comparing surface topography obtained by 3DKPM to a well-characterized topography. Several ZnO MWs ranging in diameter from 0.5 to 1.25 μm were dispersed flat on a Si substrate with sputtered 20–30 nm Au overlayer. The topography of each MW on the Si substrate was then precisely characterized by calibrated raster-scanning intermittent contact AFM. 3DKPM maps were then acquired transverse across the MW axes insuring that the tip approached closer than z_0 to the surface, i.e., the oscillating cantilever was certainly

contacting the surface intermittently at the minimum z achieved on each approach. Tip oscillation phase shift φ decreases monotonically with decreasing z (Figure 1b) until the tip snaps in to constant contact with the surface and tip oscillation amplitude becomes zero. Since decreases monotonically without any discontinuous feature clearly showing the onset of tip-surface contact, the minimum $\Delta\phi$ value that accurately reproduced the previously determined sample topography was the lower limit on $\Delta\phi$ (upper limit on z_0), which was determined to be $\Delta\phi \sim 3°$. Note that tip oscillation amplitude similarly decreases near the surface, but the degree of which was found to be strongly dependent on local $[V_{abs} + (\chi_{tip}-\chi_s)]$ and other sample properties while ϕ was nearly independent, making ϕ a more reliable metric of z_0 for the purposes of 3DKPM. The second method determined upper limits on $\Delta\phi$ by the onset of physically unrealistic spatial potential distribution $V(z)$ near the surface of an Au electrode standard sample. Physically unrealistic $V(z)$ was evidenced by, e.g., discontinuities and/or deviations from monotonicity (to which $G(z)$ must conform in the presence of a uniform surface potential, according to electrostatic principles). The onset of clearly erroneous $V(z)$ was observed in a range of $\Delta\phi$ from ~6° to ~15°, though it is probable that deviations from the correct $V(z)$ occur at lower $\Delta\phi$ (higher z). We therefore conservatively chose $\Delta\phi = 3°$ for $V(z_0)$ truncation.

ZnO MW Characterization by 3DKPM: Characterization of ZnO MW on Au channel substrate was performed as described in Section 4. The electrode bias voltage of $V_{MW} = 5$ V was selected to encourage local depletion of mobile carriers in the MW while maintaining a background potential well below the maximum V_{DC} that the KPM system can apply (10 V) to avoid saturation of the KPM measurement. The Au channel substrate was oriented such that the carrier chip and cantilever of the AFM tip was positioned over the *GND* electrode to minimize strong interaction with the V_{MW} electrode and obtain more precise measurement of V_S.[30,33,40,44] The direction of V_{MW} was then switched when rotating the sample for confirmation of symmetrical AFM tip sensitivity and quantified 3DKPM measurements were performed near the GND electrode as described previously.

Further Details: SKPM images showing disruption of surface potential measurement on typical ZnO MW due to high topography variation, 3DKPM images showing method of removing work function-induced potential for measurement calibration, and optical micrographs of ZnO MWs in the strained configurations from which piezoelectric potential measurements by 3DKPM methods were obtained and are available in the Supporting Information.

Supporting Information

Supporting Information is available from the Wiley Online Library or from the author.

FULL PAPER

[1] Y. Qin, X. Wang, Z. L. Wang, *Nature* **2008**, *451*, 809–813.

[2] X. Wang, Y. Gao, Y. Wei, Z. L. Wang, *Nano Res.* **2009**, *2*, 177–182.

[3] X. Wang, J. Song, J. Liu, Z. L. Wang, *Science* **2007**, *316*, 102–105.

[4] Z. L. Wang, J. Song, *Science* **2006**, *312*, 242–246.

[5] Z. Wang, J. Hu, M.-F. Yu, *Appl. Phys. Lett.* **2006**, *89*, 263119.

[6] Z. Wang, A. P. Suryavanshi, M.-F. Yu, *Appl. Phys. Lett.* **2006**, *89*, 082903.

[7] Z. Wang, J. Hu, A. P. Suryavanshi, K. Yum, M.-F. Yu, *Nano Lett.* **2007**, *7*, 2966–2969.

[8] S. Xu, B. J. Hansen, Z. L. Wang, *Nat. Commun.* **2010**, *1*, 1–5.

[9] X. Chen, S. Xu, N. Yao, Y. Shi, *Nano Lett.* **2010**, *10*, 2133–2137.

[10] C. Chang, V. H. Tran, J. Wang, Y.-K. Fuh, L. Lin, *Nano Lett.* **2010**, *10*, 726–731.

[11] C. Sun, J. Shi, D. J. Bayerl, X. Wang, *Energy Environ. Sci.* **2011**, *4*, 4508–4512.

[12] Z. Gao, J. Zhou, Y. Gu, P. Fei, Y. Hao, G. Bao, Z. L. Wang, *J. Appl. Phys.* **2009**, *105*, 113707.

[13] Y. Zhang, Y. Hu, S. Xiang, Z. L. Wang, *Appl. Phys. Lett.* **2010**, *97*, 033509.

[14] X. Wang, J. Song, Z. L. Wang, *J. Mater. Chem.* **2007**, *17*, 711–720.

[15] Z. L. Wang, *Nano Today* **2010**, *5*, 540–552.

[16] S. Bai, W. Wu, Y. Qin, N. Cui, D. J. Bayerl, X. Wang, *Adv. Funct. Mater.* **2011**, DOI: 10.1002/adfm.201101319.

[17] Q. Yang, X. Guo, W. Wang, Y. Zhang, S. Xu, D. H. Lien, Z. L. Wang, *ACS Nano* **2010**, *4*, 6285–6291.

[18] Z. L. Wang, *J. Phys. Chem. Lett.* **2010**, *1*, 1388–1393.

[19] Y. Hu, Y. Chang, P. Fei, R. L. Snyder, Z. L. Wang, *ACS Nano* **2010**, *4*, 1234–1240.

[20] Y. Gao, Z. L. Wang, *Nano Lett.* **2007**, *7*, 2499–2505.

[21] Y. Gao, Z. L. Wang, *Nano Lett.* **2009**, *9*, 1103–1110.

[22] G. Mantini, Y. Gao, A. D'Amico, C. Falconi, Z. L. Wang, *Nano Res.* **2009**, *2*, 624–629.

[23] M. A. Schubert, S. Senz, M. Alexe, D. Hesse, U. Gosele, *Appl. Phys. Lett.* **2008**, *92*, 122904.

[24] C. Sun, J. Shi, X. Wang, *J. Appl. Phys.* **2010**, *108*, 034309.

[25] A. K. Tagantsev, *Sov. Phys. JETP* **1985**, *61*, 1246–1254.

[26] M. S. Majdoub, P. Sharma, *Phys. Rev. B* **2008**, *78*, 121407.

[27] R. Agrawal, H. D. Espinosa, *Nano Lett.* **2011**, *11*, 786–790.

[28] X. Chen, S. Xu, N. Yao, W. Xu, Y. Shi, *Appl. Phys. Lett.* **2009**, *94*, 253113.

[29] K. Kusiaku, Ł. Borowik, D. Théóron, T. Meélin, *Appl. Phys. Lett.* **2010**, *96*, 103119.

[30] D. S. H. Charrier, M. Kemerink, B. E. Smalbrugge, T. de Vries, R. A. J. Janssen, *ACS Nano* **2008**, *2*, 622–626.

[31] S. Hudlet, M. Saint Jean, B. Roulet, J. Berger, C. Guthmann, *J. Appl. Phys.* **1994**, *77*, 3308–3314.

[32] H. O. Jacobs, P. Leuchtmann, O. J. Homan, A. Stemmer, *J. Appl. Phys.* **1998**, *84*, 1168–1173.

[33] G. Koley, M. G. Spencer, H. R. Bhangale, *Appl. Phys. Lett.* **2001**, *79*, 545–547.

[34] S. Sadewasser, C. Leendertz, F. Streicher, M. C. Lux-Steiner, *Nanotechnology* **2009**, *20*, 505503.

[35] U. Zerweck, C. Loppacher, T. Otto, S. Grafström, L. M. Eng, *Phys. Rev. B* **2005**, *71*, 125424.

[36] B. D. Huey, D. Lisjak, D. A. Bonnell, *J. Am. Ceram. Soc.* **1999**, *82*, 1941–1944.

[37] B. Polyakov, R. Krutokhvostov, A. Kuzmin, E. Tamanis, I. Muzikante, I. Tale, *Eur. Phys. J. Appl. Phys.* **2010**, *51*, 21201.

[38] Y. Rosenwaks, R. Shikler, T. Glatzel, S. Sadewasser, *Phys. Rev. B* **2004**, *70*, 085320.

[39] Y. Wu, M. A. Shannon, *Rev. Sci. Instrum.* **2006**, *77*, 043711.

[40] G. Elias, T. Glatzel, E. Meyer, A. Schwarzman, A. Boag, Y. Rosenwaks, *Beilstein J. Nanotechnol.* **2011**, *2*, 252–260.

[41] K. Okamoto, Y. Sugawara, S. Morita, *Appl. Surf. Sci.* **2002**, *188*, 381–385.

[42] E. Strassburg, A. Boag, Y. Rosenwaks, *Rev. Sci. Instrum.* **2005**, *76*, 083705.

[43] T. Machleidt, E. Sparrer, D. Kapusi, K.-H. Franke, *Meas. Sci. Technol.* **2009**, *20*, 084017.

[44] A. Blumel, H. Plank, A. Klug, E. Fisslthaler, M. Sezen, W. Grogger, E. J. W. List, *Rev. Sci. Instrum.* **2010**, *81*, 056107.

[45] H. O. Jacobs, H. F. Knapp, A. Stemmer, *Rev. Sci. Instrum.* **1999**, *70*, 1756–1760.

[46] R. Garcia, R. Perez, Â. Pe, R. Garcō, *Surf. Sci. Rep.* **2002**, *47*, 197–301.

[47] X. Zhao, H. Dankowicz, *J. Comput. Nonlinear Dyn.* **2006**, *1*, 109–115.

[48] H. Bielefeldt, F. J. Giessibl, *Surf. Sci. Lett.* **1999**, *440*, 863–867.

[49] O. P. Behrend, L. Odoni, J. L. Loubet, N. A. Burnham, *Appl. Phys. Lett.* **1999**, *75*, 2551–2553.

[50] H. L. Mosbacker, Y. M. Strzhemechny, B. D. White, P. E. Smith, D. C. Look, D. C. Reynolds, C. W. Litton, L. J. Brillson, *Appl. Phys. Lett.* **2005**, *87*, 012102.

[51] H. L. Mosbacker, C. Zgrabik, M. J. Hetzer, A. Swain, D. C. Look, G. Cantwell, J. Zhang, J. J. Song, L. J. Brillson, *Appl. Phys. Lett.* **2007**, *91*, 072102.